ACS OMEGA

http://pubs.acs.org/journal/acsodf

Article

Highly Efficient Solar Light Driven g-C_3N_4@$Cs_{0.33}WO_3$ Heterojunction for the Photodegradation of Colorless Antibiotics

Aster Aberra Tessema, Chang-Mou Wu,* and Kebena Gebeyehu Motora

Cite This: *ACS Omega* 2022, 7, 38475−38486

Read Online

ACCESS | Metrics & More | Article Recommendations | Supporting Information

ABSTRACT: This study facilitates the synthesis of a graphitic carbon nitride/cesium tungsten oxide (g-C_3N_4@$Cs_{0.33}WO_3$) heterojunction using a solvothermal method. The photocatalytic activities of the prepared samples were examined for the photodegradation of colorless antibiotics, namely tetracycline, enrofloxacin, and ciprofloxacin, as well as cationic and anionic dyes, such as methyl orange, rhodamine B, neutral red, and methylene blue, under full-spectrum solar light. We have purposely selected different kinds of wastewater pollutants of colorless antibiotics and cationic and anionic organic dyes to investigate the potential application of this heterojunction toward different groups of water pollutants. The results revealed that the g-C_3N_4@$Cs_{0.33}WO_3$ heterojunction showed an outstanding photocatalytic activity toward all the pollutants with concentrations of 20 ppm each at pH 3 by photocatalytically removing 97% of tetracycline within 3 h, 98% of enrofloxacin within 2 h, 97% of ciprofloxacin within 2.25 h, 98% of methylene blue in 1 h, 99% of rhodamine B within 2 h, 99% of neutral red in 1.25 h, and 95% of methyl orange in 2 h. These findings indicate that the developed photocatalyst possesses excellent photocatalytic properties toward seven different water pollutants that make it a universal photocatalyst. The developed g-C_3N_4@$Cs_{0.33}WO_3$ oxide heterojunction also presented a photocatalytic performance better than those of reported solar light active photocatalysts for photodegradation of rhodamine B and tetracycline. The efficient photocatalytic performance of the heterojunction can be ascribed to its extended light-absorbing ability, effective charge separation and fast charge transfer properties, and a high surface area. Moreover, an active species detection experiment also confirmed that superoxide radicals, hydroxyl radicals, and holes played significant roles in the photocatalysis of the organic dyes and tetracycline.

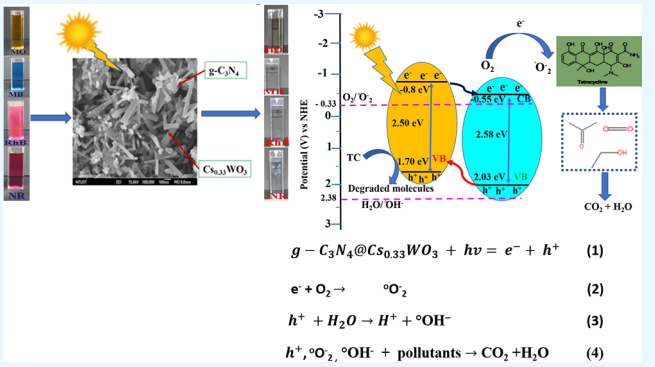

1. INTRODUCTION

Currently, environmental pollution and energy shortages have become major issues worldwide and immense efforts are being made to address them.[1] Among the several types of environmental pollution, water pollution caused by antibiotics and organic dyes is a major problem that requires immediate action. Tetracycline (TC) is one among the various types of antibiotics used in daily life to prevent and treat microbial infections.[2] It is widely utilized because of its low cost and the broad antibacterial spectrum. It is nonbiodegradable and cannot be absorbed by the animal intestine, and 90% of it is excreted into the environment, which causes environmental pollution and affects the health of living organisms.[3] Therefore, the development of an effective and efficient method for its removal is very crucial. Other types of water pollutants are organic dye effluents that are released from different industries and have low biodegradability, high levels of chemical oxygen demand, and harmful effects on human health and the environment.[4,5] Therefore, their presence is a global challenge to society and needs to be eliminated to achieve a conducive and safe environment. Thus, the development of an effective, simple, low-cost, and efficient method for removing these pollutants is essential. Previously, different methods, including adsorption, Fenton oxidation, biological filtration, chemical precipitation, photocatalysis, and ozone oxidation, have been developed for wastewater treatments.[6−10] Among these methods, photocatalysis has received significant attention[11] due to its simple operation strategy and high efficiency as well as low cost, power consumption, and eco-friendliness.[12,13] Therefore, the development of suitable and effective photocatalysts is required for environmental remediation.[14]

Solar energy is an economical, abundant, clean, renewable, and green source of energy. The sun provides a continuous and intense light energy to the surface of the earth and is the most promising renewable source of energy for environmental treatments.[15] The total solar energy comprises ultraviolet

Received: June 13, 2022
Accepted: October 4, 2022
Published: October 20, 2022

(UV), visible (Vis), and near-infrared (NIR) light, which constitutes 5%, 46%, and 49%, respectively.[16−18] However, most conventional photocatalysts, such as TiO_2, ZnO, Ag_3VO_4, MoS_2, BiS_2, TiO_2@graphene, Pt/Bi@TiO_2, GO@ZnO, D-g-C_3N_4@Bi_5O_7I, TiO_2@SiO_2@Fe_3O_4,[19−22] and Fe_3O_4, are only active in UV and Vis light or in a combination of the two, which constitutes only 5% or 50% of the solar light. This leaves the NIR light unutilized, which constitutes 50% of the solar spectrum. Therefore, the development of solar light active photocatalysts that can absorb full-spectrum solar light from NIR−Vis−UV for environmental remediation is crucial.[23]

Previous studies have found that the formation of heterostructures from different materials that absorb in the different regions of the solar light spectrum can improve the utilization of solar energy and enhance the photocatalytic activity for wastewater treatments. Therefore, the design and selection of suitable materials to form heterostructures that can absorb full-spectrum solar light are necessary. Interestingly, tungsten bronze based materials M_xWO_3 ($0 < x < 1$, M = Cs, Rb, K, Na, Li) are suitable candidates for this purpose due to their excellent NIR and UV light absorption properties.[7,24] In particular, $Cs_{0.33}WO_3$ has attracted attention in various fields, such as water evaporation,[25] photocatalysis,[26] gas sensors,[27] smart window coatings, and photothermal ablation cancer treatments,[25,28] due to its outstanding NIR light absorption property. The mixed-valence W^{5+} and W^{6+} as well as large oxygen vacancies make cesium tungsten oxide a suitable material for photocatalysis. Nevertheless, $Cs_{0.33}WO_3$ suffers from Vis light absorption, which hinders its use as a solar light photocatalyst.[25] Thus, it is mandatory to select materials that have excellent Vis light absorption properties to develop photocatalyst heterostructures to enable the efficient utilization of full-spectrum solar light.[16]

Recently, graphitic carbon nitride (g-C_3N_4), which is a metal-free semiconductor, has received considerable attention in the field of photocatalysis owing to its eco-friendliness, simple preparation method, biocompatibility, high stability, moderate band gap, low cost, and excellent Vis light absorption.[29] Due to these merits, it is being applied for the photodegradation of organic pollutants, CO_2 reduction,[30] and water splitting in environmental remediation. However, it suffers from the inefficient utilization of the full-spectrum solar light, small specific surface area, easy aggregation of nanosheets, and fast recombination of photogenerated charge carriers that hinder its use in practical applications.[31] Various methods have been developed to overcome these drawbacks, among which heterojunction formation with suitable materials is a promising strategy to improve the photocatalytic activity.[32] For instance, different types of heterojunctions such as but not limited to g-C_3N_4@WO_3,[33] UiO-66@g-C_3N_4,[34] Co_3O_4@g-C_3N_4,[35] and red phosphor@g-C_3N_4 have been developed and presented excellent photocatalytic performance compared to their respective bare materials. Different $Cs_{0.33}WO_3$-based heterostructure photocatalysts such as CdS@$Cs_{0.33}WO_3$,[36] SiO_2@$Cs_{0.33}WO_3$,[37] ZnO@$Cs_{0.33}WO_3$,[38] and AgBr@$Cs_{0.33}WO_3$[39] have also been developed and their findings reveal that the heterostructure showed outstanding photocatalytic properties compared with the two pristine materials. Previous works have been reported where $Cs_{0.33}WO_3$[16,24] was utilized as a UV- and NIR-absorbing photocatalyst. By taking advantage of the excellent UV and NIR absorption property of $Cs_{0.33}WO_3$, we have developed a full-spectrum solar light active g-C_3N_4@$Cs_{0.33}WO_3$ heterojunction photocatalyst for antibiotic degradation. Herein, g-C_3N_4 was chosen due to its good visible light absorbing property, eco-friendliness,[40] suitable band-gap energy,[41] lack of metal, and good stability.[42] Previously, Gu et al. developed a g-C_3N_4@$Cs_{0.33}WO_3$ heterojunction and it exhibited excellent photocatalytic activity for CO_2 reduction,[26] which shows its potential applicability in environmental remediation. However, we report for the first time the photocatalytic activity of the g-C_3N_4@$Cs_{0.33}WO_3$ heterojunction on the photodegradation of colored and colorless pollutants under solar light irradiation.

The limited full-spectrum solar light absorption properties of most of the developed photocatalysts are the main drawbacks in the utilization of all the irradiated solar light region for environmental remediation. In this study, a full-spectrum solar light active g-C_3N_4@$_{CsCs0.33}WO_3$ heterojunction was developed via a solvothermal method by taking into account the excellent visible light absorbing property of g-C_3N_4 and outstanding UV as well as NIR optical properties of $Cs_{0.33}WO_3$. The photocatalytic properties of the fabricated heterojunction have been demonstrated toward the photodegradation of colorless antibiotics, namely tetracycline (TC), ciprofloxacin, and enrofloxacin, as well as cationic and anionic dyes. Moreover, the effect of experimental parameters such as pH, concentration of pollutant, and catalyst dosage on the photocatalytic performance of the developed photocatalyst was investigated. The photodegradation of intermediate products was also systematically studied. Based on the experimental findings, a possible photocatalytic mechanism for the photocatalytic performance of the fabricated g-C_3N_4@$Cs_{0.33}WO_3$ heterojunction is proposed.

2. MATERIALS AND METHODS

2.1. Materials. Tungsten(VI) chloride (99.9%, Acros, New Jersey, USA), Melamine (99%. Poland), cesium hydroxide (99.9%, Alfa Aesar, Wardhill, MA, USA), anhydrous ethanol (99.5%, ECOs), glacial acetic acid (AENCORE, Surrey Hills, Australia), rhodamine B (98+%), methylene blue (99%), methyl orange (99%), tetracycline (98), enrofloxacin (99+%), and ciprofloxacin (98+%) (Sigma-Aldrich, New Jersey, USA) were purchased from the suppliers indicated.

2.2. Synthesis of g-C_3N_4@$Cs_{0.33}WO_3$ Heterojunction. First, g-C_3N_4 was synthesized from melamine according to the method described in our previously published study.[25] Thereafter, the desired amount of g-C_3N_4 was dissolved in 80 mL of ethanol and stirred for 1 h. Subsequently, 0.595 g of WCl_6 was added to the above solution, and the mixture was stirred until a homogeneous solution was obtained. Afterward, 0.13 g of $CsOH·H_2O$ was introduced and the mixture was stirred further for 10 min. Then, 20 mL of glacial acetic acid was added and a solvothermal reaction was allowed to occur for 20 h at 240 °C in an autoclave. After the reaction was completed, the autoclave was cooled to room temperature naturally, and the obtained product was washed four times with ethanol and dried in an oven at 60 °C for 8 h.[24]

2.3. Characterizations. The optical properties of the samples were investigated using UV−Vis−NIR spectrophotometry (JASCO V 670, Tokyo, Japan). The morphologies of the samples were studied by field-emission scanning electron microscopy (FESEM, JSM 6500F, JEOL Tokyo, Japan), and an N_2 adsorption measurement was done at 77 K to determine the specific surface area of the sample using a Quantachrome iQ-MP gas adsorption analyzer (BEL JAPAN, INC.). The concentrations of the pollutants were studied using UV−Vis−

https://doi.org/10.1021/acsomega.2c03675
ACS Omega 2022, 7, 38475−38486

NIR spectrophotometry in the wavelength range of 200−800 nm. The photocurrent response tests and electrochemical impedance spectroscopy (EIS) were performed using a 5000 electrochemical workstation (Technology Corp., Taipei, Taiwan). The total organic carbon was investigated with a Vario TOC select Elemenetar instrument, and the intermediate products were studied by a gas chromatograph−mass spectrometer detector (5977B GC/MSD and 7890B GC) system.

2.4. Study of Photocatalytic Properties. The photocatalytic activities of the as-prepared photocatalysts were evaluated for the photodegradation of pollutants, such as TC, enrofloxacin, ciprofloxacin, methylene blue (MB), rhodamine B (Rh B), red dye, and methyl orange (MO) under full solar light illumination. Typically, 20 mg of the photocatalyst was dispersed in 100 mL of a solution containing 20 ppm of each pollutant. Before photocatalysis, the mixture was stirred in the dark for 30 min to attain an adsorption−desorption equilibrium. Then, a Xe lamp (500 W Prosper Optoelectronic, Co., Ltd., Taipei, Taiwan) with a wavelength range of 250−2500 nm was used as the light source. The distance between the lamp and photocatalysis reactor was 35 cm, and the optical intensity of solar light was 0.25 W/cm^2. The light was irradiated for 2 h in the case of MO, Rh B, and enrofloxacin, for 1 h in the case of MB, and for 3, 2.25, and 1.25 h for TC, ciprofloxacin, and NR, respectively. A 4 mL portion of the solution was taken every 15 min and centrifuged. The concentration of each pollutant left in the supernatant solution was analyzed using a UV−vis−NIR spectrometer (V-670, JASCO, Tokyo Japan).[43−45] Finally, the degradation efficiencies of organic dyes and TC were calculated based on eq 1[46−51]

$$\text{degradation efficiency}\ (\%) = \frac{C_0 - C_t}{C_0} \times 100 \quad (1)$$

where C_t is the concentration at irradiation time t and C_0 is the initial concentration of the pollutant.

2.5. Photoelectrochemical Measurements. EIS was used in a conventional three-electrode configuration. The as-prepared samples were cast on 1 × 1 cm^2 titanium, which served as the working electrode, and a Ag/AgCl electrode, platinum electrode, and 0.1 M KCl solution were used as the reference electrode, counter electrode, and electrolyte, respectively. Benzoquinone (BQ), isopropanol (IPA), and ethylenediaminetetraacetic acid (EDTA) were used as superoxide radical, hydroxyl radical, and hole scavengers, respectively, in the active species study.

3. RESULTS AND DISCUSSION

3.1. Characterization of the g-C_3N_4@$Cs_{0.33}WO_3$ Heterojunction. Figure 1a displays the FESEM image of the g-C_3N_4@$Cs_{0.33}WO_3$ heterojunction, which demonstrates that the g-C_3N_4 nanoparticle (shown in red) is adhered to the surface of the $Cs_{0.33}WO_3$ nanorods (encircled in yellow), indicating a good contact between g-C_3N_4 and $Cs_{0.33}WO_3$. The energy-dispersive X-ray spectrum (EDS) presented in Figure 1b also confirms the existence of Cs, W, O, N, and C in the g-C_3N_4@$Cs_{0.33}WO_3$ heterojunction, which shows the coexistence of $Cs_{0.33}WO_3$ and g-C_3N_4. The crystal structures of the fabricated g-C_3N_4, $Cs_{0.33}WO_3$, and g-C_3N_4@$Cs_{0.33}WO_3$ were investigated and reported in our previous study.[25] The actual atomic and mass percentages of elements in the developed $Cs_{0.33}WO_3$@g-C_3N_4 heterojunction (Figure 1b inset) were also almost the same as the theoretical mass and atomic percentages of each element used in the synthess, that confirms the successful fabrication of the heterojunction.

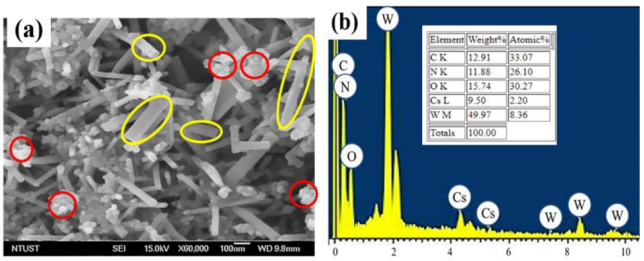

Figure 1. (a) FESEM image and (b) corresponding EDS spectrum of the g-C_3N_4@$Cs_{0.33}WO_3$ heterojunction.

3.2. Photoelectrochemical and Optical Analyses. Figure 2a shows the EIS results of g-C_3N_4, $Cs_{0.33}WO_3$, and the g-C_3N_4@$Cs_{0.33}WO_3$ heterojunction, and the figure depicts that the semicircle radius of the g-C_3N_4@$Cs_{0.33}WO_3$ heterojunction is much smaller than those of g-C_3N_4 and $Cs_{0.33}WO_3$, indicating the excellent charge transfer of the heterojunction. The photoluminescence (PL) spectra (Figure 2b) indicated that the g-C_3N_4@$Cs_{0.33}WO_3$ heterojunction presented the lowest PL peak intensity followed by $Cs_{0.33}WO_3$, which shows the suppression of photogenerated electron−hole recombination and efficient charge separation, which is crucial for achieving an effective photocatalysis. In contrast, g-C_3N_4 exhibited strong PL peaks, indicating a high recombination rate of hole−electron pairs in g-C_3N_4, which is not ideal for an effective photocatalysis. The photocurrent response results displayed in Figure 2c also indicate that the g-C_3N_4@$Cs_{0.33}WO_3$ heterojunctions exhibit strong photocurrent responses compared to those of the bare materials, which indicates that the heterojunction possesses an excellent light absorption and conversion efficiency. The enhancement of the photocurrent response shows that the heterojunction can efficiently generate and transfer photogenerated charge carriers, which causes efficient electron−hole pair separation

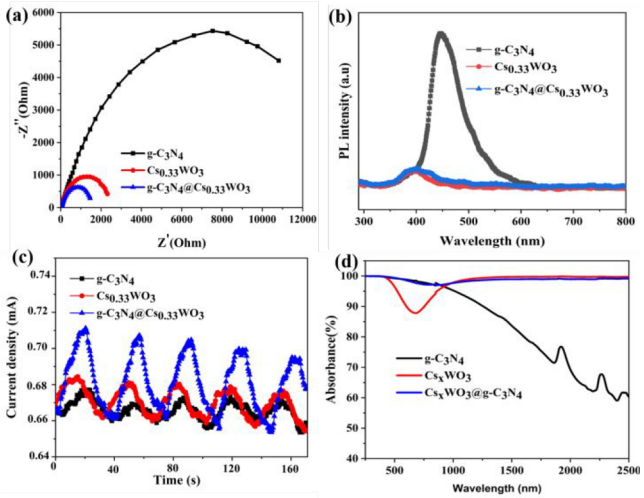

Figure 2. (a) EIS, (b) photocurrent response, (c) PL spectra, and (d) DRS spectra of $Cs_{0.33}WO_3$, g-C_3N_4, and the g-C_3N_4@$Cs_{0.33}WO_3$ heterojunction.

https://doi.org/10.1021/acsomega.2c03675
ACS Omega 2022, 7, 38475−38486

and a high photocatalytic performance.[6] The optical properties of the synthesized samples were also investigated in full-spectrum solar light (UV−vis−NIR region), and the results (Figure 2d) show that g-C_3N_4 exhibits a strong optical absorption in the Vis region but limited optical absorption in the UV and NIR regions. $Cs_{0.33}WO_3$ exhibited significant NIR and UV light absorption properties, which are crucial for full-spectrum solar light absorption. Consequently, the developed g-C_3N_4@$Cs_{0.33}WO_3$ heterojunction demonstrated Vis, UV, and NIR light absorption capabilities throughout the solar spectrum, which is very important for improving the photocatalytic activity.

Moreover, the band gap of the photocatalyst, which is an important parameter in photocatalysis, was determined by using the Kubelka−Munk formula[52] from DRS, and the plots of $(\alpha h\nu)^{1/2}$ versus $h\nu$, where h, α, and ν denote Planck's constant, absorption coefficient, and light frequency, respectively, are displayed in Figure 3a−c. From the results, the

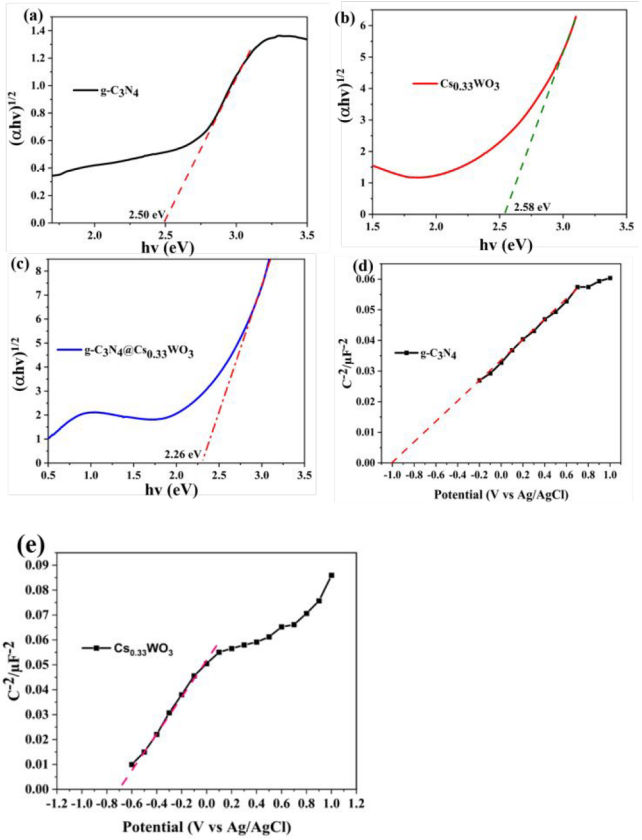

Figure 3. (a−c) Band gaps for g-C_3N_4, $Cs_{0.33}WO_3$, and g-C_3N_4@$Cs_{0.33}WO_3$ respectively. (d, e) Mott−Schottky plots of g-C_3N_4 and $Cs_{0.33}WO_3$, respectively.

calculated band gap energies (E_g) of g-C_3N_4, $Cs_{0.33}WO_3$, and g-C_3N_4@$Cs_{0.33}WO_3$ were 2.50, 2.58, and 2.26 eV, respectively. The flat-band potentials of g-C_3N_4 and $Cs_{0.33}WO_3$ were determined by the Mott−Schottky method, and g-C_3N_4 (Figure 3d) as well as $Cs_{0.33}WO_3$ (Figure 3e) demonstrated positive slopes, which indicated that both materials are n-type semiconductors.[46] As can be seen from the linear extrapolation of the results to the x intercepts of Figure 3, the flat band potentials versus an Ag/AgCl electrode for $Cs_{0.33}WO_3$, and g-C_3N_4 are −0.75, and −1.0 V, respectively.[53] By using the formula for the normal hydrogen electrode $E_{NHE} = E_{Ag/AgCl} +$ 0.197 V,[54,55] the corresponding values vs NHE of $Cs_{0.33}WO_3$, and g-C_3N_4 are −0.55, and −0.8 V, respectively. The conduction band (CB) potentials of n-type semiconductors are almost equal to the flat-band potentials. Therefore, the corresponding CBs of $Cs_{0.33}WO_3$ and g-C_3N_4 are −0.55 and −0.8 eV, respectively, as calculated according to the formula $E_{VB} = E_g + E_{CB}$,[56] in which the determined valence bands (VBs) of $Cs_{0.33}WO_3$ and g-C_3N_4 are 2.02 and 1.7 eV versus the normal hydrogen electrode (NHE), respectively. The E_g values of g-C_3N_4 and $Cs_{0.33}WO_3$ are 2.50 and 2.58 eV, respectively, as presented in Figure 3a,b.

Moreover, the specific surface areas and pore size N_2 adsorption−desorption isotherms of the fabricated samples were investigated, and the results given in Figure 4 show that

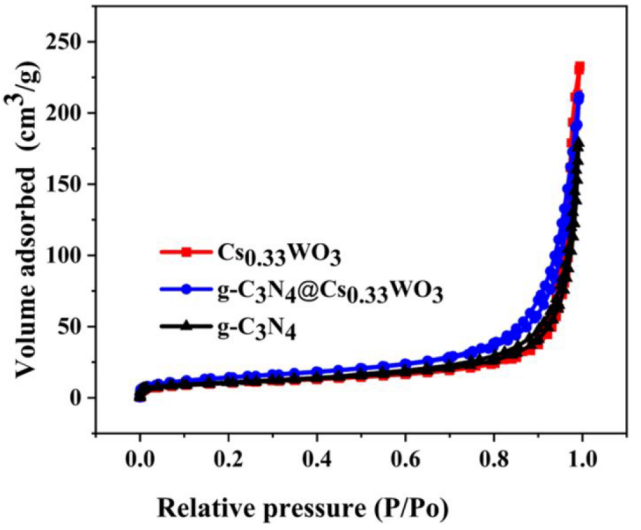

Figure 4. N_2 adsorption−desorption isotherms of $Cs_{0.33}WO_3$, g-C_3N_4@$Cs_{0.33}WO_3$, and g-C_3N_4.

all of the photocatalysts presented type IV hysteresis loops according to the Brunauer−Deming−Deming−Teller classification.[27] The calculated specific surface area, pore diameter, and pore volume are also displayed in Table 1, and the results

Table 1. BET Specific Surface Areas, Pore Diameters, and Pore Volumes of Photocatalysts

photocatalyst	specific BET surface area (m^2/g)	pore diameter (nm)	pore volume (cm^3/g)
g-C_3N_4	37.29	28.15	0.26
$Cs_{0.33}WO_3$	36.64	36.49	0.33
g-C_3N_4@$Cs_{0.33}WO_3$	51.74	23.84	0.30

show that the synthesized g-C_3N_4@$Cs_{0.33}WO_3$ heterojunction presented the highest specific surface area of 51.74 m^2/g as compared to those of the bare materials $Cs_{0.33}WO_3$ and g-C_3N_4. This improved surface area provides a large active site for the adsorption of pollutants on the photocatalyst, further enhancing the photocatalytic activity of the heterojunctions.[57]

3.3. Study of Photocatalytic Activity on Organic Dyes. The photocatalytic activities of the as-synthesized photocatalysts were investigated for different types of pollutants composed of cationic and anionic organic dyes. First, the photocatalytic properties of the fabricated photocatalysts toward the anionic dye MO were investigated, and the

https://doi.org/10.1021/acsomega.2c03675
ACS Omega 2022, 7, 38475−38486

results shown in Figure 5a indicate that the g-C_3N_4@$Cs_{0.33}WO_3$ heterojunction exhibited excellent photocatalytic

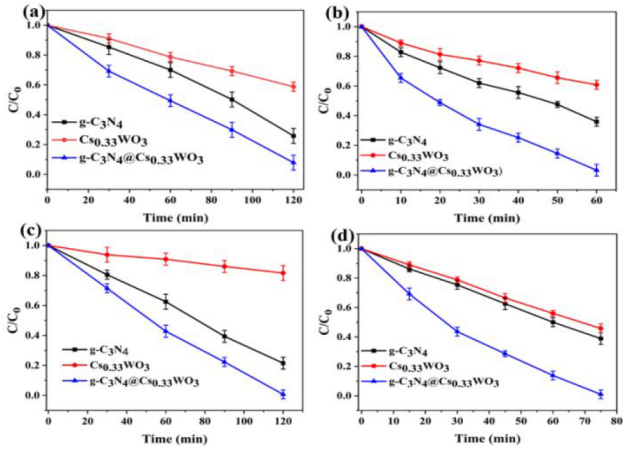

Figure 5. Photocatalytic degradation efficiency of the as-prepared samples on (a) MO, (b) MB, (c) Rh B, and (d) NR, under solar light irradiation.

activity by degrading 95.4% within 2 h under solar light irradiation. $Cs_{0.33}WO_3$ and g-C_3N_4 degraded only 41.4% and 73.7% of MO, respectively, under the same conditions. Moreover, the universal applicability of the developed photocatalysts was evaluated by applying them to different cationic dyes and Figure 5b depicts that the g-C_3N_4@$Cs_{0.33}WO_3$ heterojunction showed excellent photocatalytic activity toward MB by degrading 98.2% of it in 1 h, whereas the photocatalytic activities of bare g-C_3N_4 and $Cs_{0.33}WO_3$ were 63.2% and 38.4%, respectively, under the same experimental conditions. Similarly, the synthesized heterojunction displayed significant photocatalytic properties toward Rh B by decomposing 99.2% of Rh B within 2 h (Figure 5c), while only 17.4% and 73.5% of Rh B were degraded by $Cs_{0.33}WO_3$ and g-C_3N_4, respectively. Figure 5d also shows that the g-C_3N_4@$Cs_{0.33}WO_3$ heterojunction possesses excellent photocatalytic activity toward the neutral red (NR) dye, and 99.3% can be decomposed in 75 min, whereas only 57.4% and 54.1% could be decomposed by g-C_3N_4 and $Cs0_{.33}WO_3$ under similar conditions, respectively. The excellent photocatalytic activity of the g-C_3N_4@$Cs_{0.33}WO_3$ heterojunction toward all pollutants compared to those of the bare g-C_3N_4 and $Cs_{0.33}WO_3$ can be ascribed to the extension of the optical absorption region, high surface area, and effective charge separation.[6] In addition, the photocatalytic performance of the developed g-C_3N_4@$Cs_{0.33}WO_3$ heterojunction was also compared with those of previously reported solar light active photocatalysts for the photodegradation of Rh B. The findings in Table 2 show that the developed g-C_3N_4@$Cs_{0.33}WO_3$ heterojunction exhibited an excellent photocatalytic performance compared to those reported in the literature. This indicates that the fabricated photocatalyst is a promising candidate for application in environmental remediation for the treatment of organic dyes and can be employed for real-life applications.

The rate of the reaction kinetics of the photocatalyst was also studied by fitting the experimental results with a pseudo-first-order reaction model according to eq 2[7]

$$-\ln(C_t/C_0) = kt \quad (2)$$

where k is the kinetic rate constant, t is the irradiation time, and C_0 and C_t are the concentrations of pollutants at time 0 and time t, respectively. Figure S1a–d shows the linear plots of $\ln(C_t/C_0)$ versus the irradiation time for MO, MB, Rh B, and red dye. The reaction rate constant (k) was calculated and is provided in Table 3. The reaction rate of the g-C_3N_4@$Cs_{0.33}WO_3$ heterojunction is faster than those of bare g-C_3N_4 and $Cs_{0.33}WO_3$ for all of the studied pollutants (MO, MB, Rh B, and NR). For example, the reaction rate kinetic constant of the heterojunction is about 1.8 times faster than that of g-C_3N_4 and is about 12 times faster than that of $Cs_{0.33}WO_3$ for the photodegradation of Rh B dye under the same experimental conditions. The improved reaction rate of the g-C_3N_4@$Cs_{0.33}WO_3$ heterojunction could be due to the large surface area, extended full-spectrum light absorbance, narrowing of the band gap, and effective charge transfer of photogenerated charge carriers.[57]

Table 3. Pseudo-First-Order Rate Constants (min^{-1}) for MO, MB, Rh B, and NR Dye Degradation under Solar Light Irradiation

	k (10^{-3} min^{-1})			
photocatalyst	MO	Rh B	MB	NR
g-C_3N_4	9.7	10.8	16.4	12.5
$Cs_{0.33}WO_3$	4.4	1.6	7.8	10.4
g-C_3N_4@$Cs_{0.33}WO_3$	19.6	19.5	40.3	31.5

To evaluate the light utilization efficiency of the developed g-C_3N_4@$Cs_{0.33}WO_3$ heterojunction, the apparent quantum efficiency (Φ) of the photocatalyst was calculated according to eq 3[62]

$$\Phi = \frac{\text{reaction rate}}{\text{incident photon flux}} \approx \frac{N_A v \, dC_A/dt}{dN_{ph}/dt} \quad (3)$$

where v is the volume of the reaction solution (L), N_A is Avogadro's number (6.022×10^{23} molecules/mol), C_A is the concentration of the reactant A (mol/L), N_{ph} is the number of photons supplied in time t, and t is reaction time. Herein, the reactant is MB.

Table 2. Comparison of the Photocatalytic Activity of the Developed g-C_3N_4@$Cs_{0.33}WO_3$ Heterojunction with Those of the Previously Reported Solar Light Photocatalysts for the Photodegradation of Rh B Dye

photocatalyst	pollutant	time (min)	light source	photodegradation (%)	ref
ZnS/Ag/$CoFe_2O_4$	Rh B	150	solar	96.5	58
MoS_2/WO_3	Rh B	120	solar	92.6	59
ZnS	Rh B	160	solar	94.0	60
TiO_2 graphene aerogel	Rh B	180	solar	91.0	61
g-C_3N_4@$Cs_{0.33}WO_3$	Rh B	120	solar	99.1	this work

https://doi.org/10.1021/acsomega.2c03675
ACS Omega 2022, 7, 38475−38486

The calculated apparent quantum efficiencies under incident light of 3×10^{15} photons/s were 2.5%, 0.85%, and 0.53% for the g-C_3N_4@$Cs_{0.33}WO_3$ nanocomposite, g-C_3N_4, and $Cs_{0.33}WO_3$ photocatalysts, respectively. This finding depicts that the g-C_3N_4@$Cs_{0.33}WO_3$ heterojunction had apparent quantum efficiency of about 3 times that of g-C_3N_4 and almost 5 times that of $Cs_{0.33}WO_3$. The heterojunction formation has largely improved the apparent quantum efficiency, which improved the photocatalytic performance of the developed material.

The total organic carbon (TOC) was investigated to evaluate the mineralization property of the g-C_3N_4@$Cs_{0.33}WO_3$ heterojunction on Rh B and TC pollutants under solar light irradiation. The finding shown in the Figure 6

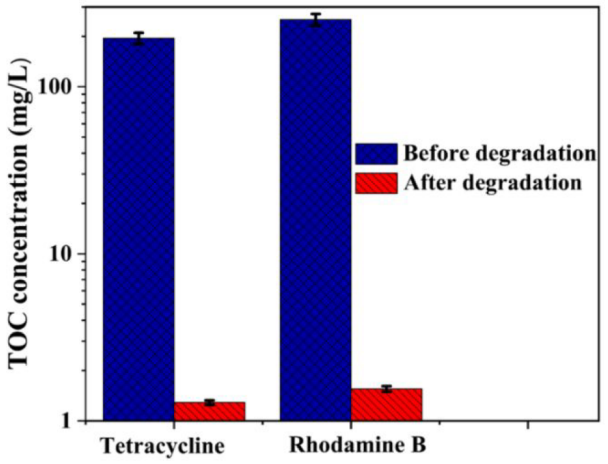

Figure 6. TOC analysis of Rh B and TC pollutants before and after their photodegradation.

presents the TOC of the Rh B before and after photocatalysis by the g-C_3N_4@$Cs_{0.33}WO_3$ heterojunction. The decrease of the TOC in the Rh B of 99.4% after photocatalysis confirms the mineralization of the Rh B into CO_2 and H_2O.[63,64] Similarly, the concentrations of TOC before and after photodegradation of TC were also determined, and the finding reveals that 99% of TOC was removed during photodegradation of TC, which confirms the excellent mineralization properties of the developed photocatalyst during photodegradation of TC.[65]

3.4. Photocatalytic Activity on Antibiotics. The photocatalytic activity of the heterojunction as well as bare samples was evaluated by photodegradation of antibiotics such as enrofloxacin, ciprofloxacin, and tetracycline under simulated solar light. The result presented in Figure 7a indicates that the g-C_3N_4@$Cs_{0.33}WO_3$ heterojunction exhibited excellent photocatalytic activity toward ciprofloxacin by degrading 98% of it within 135 min under solar light irradiation. However, $Cs_{0.33}WO_3$ and g-C_3N_4 degraded only 56% and 64.2% of ciprofloxacin, respectively, under the same experimental conditions. Moreover, the as-prepared g-C_3N_4@$Cs_{0.33}WO_3$ heterojunction also displayed outstanding photocatalytic properties toward enrofloxacin by decomposing 97.1% of it within 2 h (Figure 7b), while only 68% and 73.5% of enrofloxacin were degraded by $Cs_{0.33}WO_3$ and g-C_3N_4, respectively. Furthermore, the g-C_3N_4@$Cs_{0.33}WO_3$ heterojunction also exhibited significant photocatalytic activity toward TC by decomposing 97% of it within 3 h (Figure 7c), whereas 83.7% and 61.8% degradations of TC were

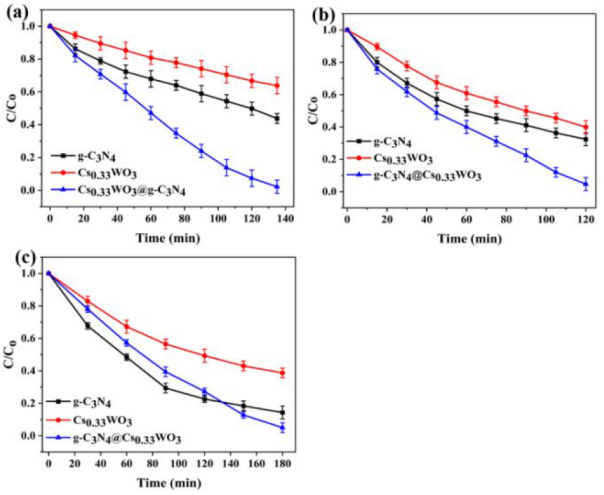

Figure 7. Photocatalytic degradation efficiency of the as-prepared samples on (a) ciprofloxacin (b) enrofloxacin, and (c) TC, under solar light irradiation.

achieved by g-C_3N_4 and $Cs_{0.33}WO_3$, respectively. Furthermore, the photocatalytic performance of the developed g-C_3N_4@$Cs_{0.33}WO_3$ heterojunction was compared with those of previously reported photocatalysts for the photodegradation of TC, and the results are displayed in Table 4. The finding displays that the developed g-C_3N_4@$Cs_{0.33}WO_3$ heterojunction shows better TC photodegradation than those reported photocatalysts.

Figure S2a−c shows the linear plots of $\ln(C_t/C_0)$ versus the irradiation time for enrofloxacin, ciprofloxacin, and TC photodegradations. The reaction rate constants (k) were calculated and are provided in Table 5. The reaction rate of the g-C_3N_4@$Cs_{0.33}WO_3$ heterojunction is faster than that of bare g-C_3N_4 and $Cs_{0.33}WO_3$ for all of the studied pollutants (enrofloxacin, ciprofloxacin, and TC). As can be seen from Table 5, the reaction rate kinetic constant for the g-C_3N_4@$Cs_{0.33}WO_3$ heterojunction is greater than those of bare g-C_3N_4 and $Cs_{0.33}WO_3$ for all of the studied colorless antibiotic pollutants. For instance, the reaction rate kinetic constant of the g-C_3N_4@$Cs_{0.33}WO_3$ heterojunction is about 2.7 times faster than that of g-C_3N_4 and 4.6 times faster than that of $Cs_{0.33}WO_3$ for the photodegradation of ciprofloxacin under the same experimental conditions.

The stability and reusability of the developed photocatalyst, which are crucial for practical applications,[57] were studied, and the results in Figure 8a,b show that the synthesized g-C_3N_4@$Cs_{0.33}WO_3$ heterojunction exhibited significant stability for the photocatalytic degradation of the cationic dye Rh B and anionic dye MO for four consecutive experiments. There was no significant decrease in the photocatalytic performance observed in the four cycles for pollutants, indicating the stability and reusability of the developed photocatalyst. These findings show that the g-C_3N_4@$Cs_{0.33}WO_3$ heterojunction possesses excellent stability for the photocatalytic degradation of cationic and anionic dyes and can be a promising candidate for practical application in environmental remediation.

3.5. Effect of Operational Parameters on Photocatalytic Properties. *3.5.1. Effect of pH on the Photocatalytic Performance.* The effects of pH on the photocatalytic performance of the developed g-C_3N_4@$Cs_{0.33}WO_3$ heterojunction was investigated, and the findings are presented

https://doi.org/10.1021/acsomega.2c03675
ACS Omega 2022, 7, 38475−38486

Table 4. Comparison of the Photocatalytic Performance of the Fabricated g-C_3N_4@$Cs_{0.33}WO_3$ Heterojunction with Those of the Previously Reported Solar Light Photocatalysts for Photodegradation of the Colorless Antibiotic TC

photocatalyst	pollutant	irradiation time (min)	light source	photodegradation efficiency (%)	ref
TiO_2 graphene aerogel	TC	180	solar	43	61
Bi_2WO_6 /TiO_2	TC	180	solar	92	66
Co-doped UiO-66	TC	180	solar	94	67
Bi_2MoO_6/WO_3	TC	180	solar	86	68
$FeNi_3$/SiO_2/CuS	TC	200	solar	81	69
g-C_3N_4@$Cs_{0.33}WO_3$	TC	180	solar	97	this work

Table 5. Pseudo-First-Order Rate Constants (min^{-1}) for Enrofloxacin, Ciprofloxacin, and TC Degradation under Solar Light Irradiation

	k (10^{-3} min^{-1})		
photocatalyst	enrofloxacin	ciprofloxacin	TC
g-C_3N_4	8.0	5.5	11.6
$Cs_{0.33}WO_3$	7.0	3.2	5.3
g-C_3N_4@$Cs_{0.33}WO_3$	15.2	14.9	14.3

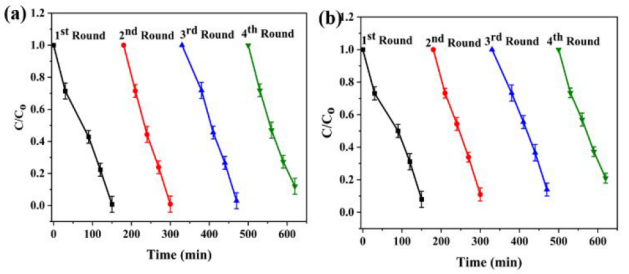

Figure 8. Cyclic stability tests for (a) Rh B and (b) MO degradation using g-C_3N_4@$Cs_{0.33}WO_3$ under solar light irradiation.

in Figure 9a,b. The result shows that the pH has a significant effect on the photocatalytic performance of the developed catalyst and the highest photodegradation efficiency (97%) was achieved for TC at pH 3 (Figure 9a). According to previous reports, TC exists mainly in three different forms based on the pH of the solution. At the more acidic pH < 3.3, it exists as TCH_3^+. When the solution pH is between 3.3 and 7.7, it exists as neutral TCH_2. For a solution of pH > 7.7 it exists as an anion, TCH^- or TCH_2^-.[70] Therefore, the adsorption of TC on the surface of the g-C_3N_4@$Cs_{0.33}WO_3$ heterojunction decreased with an increase in the pH of the solution. This was due to the fact that above pH 7 TC is negatively charged and the catalyst charge is also negative. There is a high repulsion interaction between the similar charges. These results decrease the TC degradation efficiency. Moreover, the effect of pH on the photodegradation of Rh B was also studied, and the result in Figure 9b depicts that the greatest amount of Rh B (99%) can be photodegraded at pH 3. This is due to the strong adsorption of the cationic form of Rh B onto the photocatalyst at pH 3 that facilitates the photodegradation efficiency.[71] The ζ potential analysis result shown in Figure S3 also indicates that the developed g-C_3N_4@$Cs_{0.33}WO_3$ heterojunction possesses a negative surface charge and the electrostatic attraction between the negatively charged photocatalyst and positively charged pollutants at lower pH facilitates fast photodegradation at pH 3.

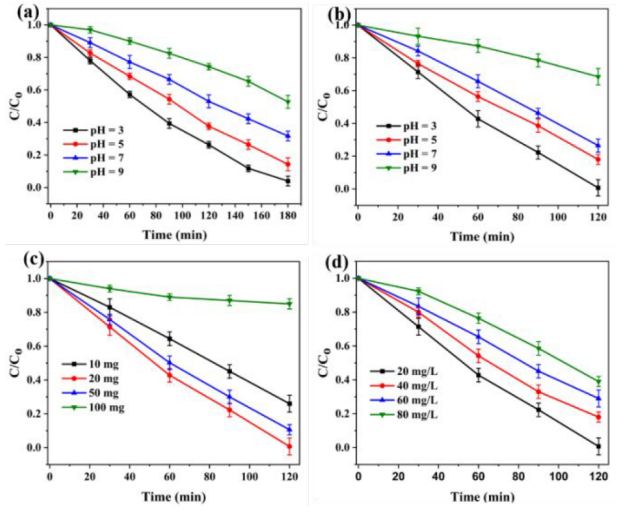

Figure 9. Effect of pH on the photodegradation of (a) TC and (b) Rh B. (c) Effect of catalyst dosage and (d) dye concentration on the photodegradation of Rh B.

3.5.2. Effect of Concentration on Photocatalytic Properties. The effect of the pollutant concentration on the photocatalytic ability of the catalyst was also evaluated, and the finding in Figure 9c shows that the photodegradation efficiency decreases as the concentration of Rh B increases. The decrease in photodegradation efficiency of the photocatalyst with an increase in pollutant concentration can be due to presence of more pollutant molecules than accessible active sites on the photocatalyst. Besides, theexistence of more dye molecules at higher dye concentrations can also decrease the amount of light that reaches the photocatalyst surface and further decreases the photocatalytic performance.[72,73] Since a 20 ppm dye concentration presented the highest photodegradation efficiency, it was selected for further study.

3.5.3. Effect of Catalyst Dosage on Photocatalytic Performance. The effect of catalyst dosage on the photodegradation of Rh B was studied by varying the amounts of catalyst from 10 to 20, 50, and 100 mg while keeping other parameters constant. Figure 9d shows that the photodegradation efficiency of Rh B sharply increased to 99% within 120 min as the catalyst dosage increased from 10 to 20 mg. However, further increments of photocatalyst dosage deceases the photodegradation efficiency. This negative effect at higher amounts of catalyst dosage is due to aggregation, photon scattering, suspension turbidity, and masking of the photosensitive surface, and thus, the hindrance of photon penetration in the solid phase decreases the photocatalytic activity.[74,75]

3.6. Identification of Intermediates and Possible Photocatalytic Mechanism. The intermediate products of the photodegradation of TC, ciprofloxacin, and enrofloxacin were investigated by using GC-MS. For the photodegradation

https://doi.org/10.1021/acsomega.2c03675
ACS Omega 2022, 7, 38475−38486

of TC, three intermediates (Table S1) were identified based on the molecular ions in the MS spectrum.[76,77] The chromatograms of the identified intermediates are shown in Figure S4. From the finding, it can be concluded that the TC photodegradation process takes place through dehydoxylation, N-demethylation, deamination, and ring opening in which the carbon−carbon bonds of TC are attacked by superoxide and hydroxyl radicals that leads to the generation of intermediates with carbonyl or hydroxyl groups.[78] The intermediate products of the ciprofloxacin photodegradation were also studied, and the GC-MS spectrum in Figure S5 presents the formation of three different intermediates during the photocatalysis reaction (Table S2). Those intermediate formations can be ascribed to cleavage of the C−C and C−N bonds.[79] During the photodegradation of ciprofloxacin, piperazine ring cleavage and decarboxylation of the quinolone ring takes place due to the attack of superoxide radicals and finally the intermediates can be converted to small molecules such as H_2O, F^-, and CO_2.[80] Moreover, the byproducts of the enrofloxacin were also investigated, and the results given in Figure S6 and Table S3 depict that six intermediates were generated during the photodegradation of enrofloxacin. The findings reveal that the photodegradation of enrofloxacin takes place via defluorination, cyclopropane and piperazine bond cleavage, and benzene and quinolone ring cleavage from the attack of photogenerated active species such as superoxide radicals, holes, and hydroxyl radicals. Then, the intermediates mineralized to smaller molecules such as NH_4^+, H_2O, and CO_2.[81−83]

To propose a photocatalytic mechanism for the photodegradation of the above pollutants, the roles of superoxide radicals, hydroxyl radicals, and holes were investigated using the respective scavengers BQ, IPA, and EDTA on the photodegradation of MO and TC. Figure 10a shows that the

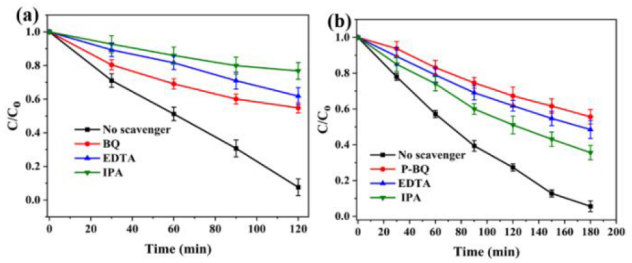

Figure 10. Active species determination for (a) MO and (b) TC.

photodegradation of MO was largely suppressed in the presence of IPA followed by EDTA and was slightly affected by BQ, which indicates that hydroxyl radicals play a major role in the photodegradation of MO followed by holes and superoxide radicals, respectively. In the case of TC photodegradation (Figure 10b), the presence of BQ largely suppressed the photodegradation and was sequentially followed by EDTA and IPA, which showed that superoxide radicals play a dominant role in the photodegradation, followed by holes and hydroxyl radicals, respectively.

Based on the above results, a possible photocatalytic mechanism for the developed g-C_3N_4@$Cs_{0.33}WO_3$ heterojunction can be proposed, as depicted in Figure 11. Accordingly, when solar light is irradiated on the photocatalyst, electrons are excited from the VBs of both materials to their respective CBs due to their suitable band gaps and

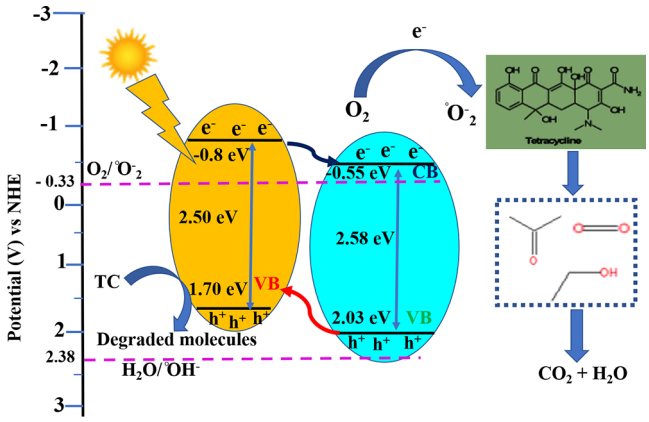

Figure 11. Proposed photocatalytic mechanism for the photocatalytic activity of g-C_3N_4@$Cs_{0.33}WO_3$ in the photodegradation of TC.

simultaneously leave holes in their respective VBs.[6] These photogenerated electrons and holes move to the surface and are responsible for photocatalysis. These photogenerated charge carriers produce reactive oxygen species (ROS), such as superoxide radicals and hydroxyl radicals, that have sufficient energies to decompose organic contaminants.[6] The irradiation of solar light will cause the excitation of electrons from the VBs of g-C_3N_4 and $Cs_{0.33}WO_3$, which leaves holes in the VBs (eq 4). Thereafter, the electrons in the CB of g-C_3N_4 transfer to the CB of $Cs_{0.33}WO_3$. Subsequently, reaction with dissolved oxygen at the surface and formation of superoxide radicals (eq 5) cause pollutant degradation, whereas the holes in the VB of $Cs_{0.33}WO_3$ transferring to the VB of g-C_3N_4 directly react with the pollutant and possess sufficient energy to degrade organic pollutants.[26,57] Thus, the generated charge carriers are responsible for the overall photocatalytic degradation of the pollutants and the heterojunction formation could enhance the separation of photogenerated charge carriers compared to pure materials, thereby resulting in an improved photocatalytic activity.[7]

$$\text{g-}C_3N_4@Cs_{0.33}WO_3 + h\nu = e^- + h^+ \quad (4)$$

$$e^- + O_2 \rightarrow O_2^{\bullet -} \quad (5)$$

$$h^+ + H_2O \rightarrow H^+ + {}^{\bullet}OH \quad (6)$$

$${}^{\bullet}OH,\ O_2^{\bullet -},\ h^+ + \text{pollutants} \rightarrow \text{degraded product} \quad (7)$$

4. CONCLUSIONS

In this study, we successfully synthesized a solar light driven g-C_3N_4@$Cs_{0.33}WO_3$ heterojunction by a solvothermal method. The developed g-C_3N_4@$Cs_{0.33}WO_3$ heterojunction photocatalyst exhibited an excellent photocatalytic performance toward colored cationic and anionic organic dyes as well as colorless enrofloxacin, ciprofloxacin, and TC antibiotics. The photocatalytic activities of g-C_3N_4@$Cs_{0.33}WO_3$ heterojunctions toward the photodegradation of MO, Rh B, MB, NR, enrofloxacin, ciprofloxacin, and TC were approximately 4.5, 12, 5, 3, 2.1, 4.6, and 2.7 times faster than those of pure $Cs_{0.33}WO_3$, respectively. This indicates that the fabricated photocatalyst can be utilized as a universal photocatalyst for the treatment of different wastewater pollutants. The developed photocatalyst also exhibited photocatalytic performance superior to those of reported solar light active

https://doi.org/10.1021/acsomega.2c03675
ACS Omega 2022, 7, 38475−38486

photocatalysts for the photodegradation of Rh B and TC. Therefore, it is an excellent photocatalyst for the photodegradation of organic dyes and colorless antibiotics under solar light. The trapping experiments revealed that superoxide radicals, hydroxyl radicals, and holes play crucial roles in determining the photocatalytic activity of the fabricated photocatalyst. Among all pollutants studied in this work, the cationic dye MB photodegraded the fastest compared to others: 98.2% of it was photodegraded within just 1 h. The result shows that the g-C_3N_4@$Cs_{0.33}WO_3$ heterojunction exhibits highest adsorption toward MB in comparison to other pollutants and this high adsorption property of the MB on the developed photocatalyst facilitated the fast photodegradation of the pollutant. The effective photocatalytic performance of the developed g-C_3N_4@$Cs_{0.33}WO_3$ could be ascribed to the extended full-spectrum light absorption, high surface area, effective charge separation of photogenerated charge carriers, and narrow band gap. Therefore, this study paves the way for environmental scientists to design an effective, low-cost, and efficient solar light active photocatalyst for environmental remediation.

■ ASSOCIATED CONTENT

Supporting Information

The Supporting Information is available free of charge at https://pubs.acs.org/doi/10.1021/acsomega.2c03675.

Identified intermediates, kinetic pseudo-first-order plots, ζ potential, and GC-MS spectra of enrofloxacin, TC, and ciprofloxacin antibiotics (PDF)

■ AUTHOR INFORMATION

Corresponding Author

Chang-Mou Wu − *Department of Materials Science and Engineering, National Taiwan University of Science and Technology, Taipei 10607, Taiwan, Republic of China;* orcid.org/0000-0001-8127-991X; Phone: +886-2-2737-6530; Email: cmwu@mail.ntust.edu.tw

Authors

Aster Aberra Tessema − *Department of Materials Science and Engineering, National Taiwan University of Science and Technology, Taipei 10607, Taiwan, Republic of China*

Kebena Gebeyehu Motora − *Department of Materials Science and Engineering, National Taiwan University of Science and Technology, Taipei 10607, Taiwan, Republic of China*

Complete contact information is available at: https://pubs.acs.org/10.1021/acsomega.2c03675

Author Contributions

A.A.T.: investigation, data curation, and writing. C.-M.W.: conceptualization, supervision, review, and editing. K.G.M.: review, editing, methodology, and investigation.

Notes

The authors declare no competing financial interest.

■ ACKNOWLEDGMENTS

The authors thank the Ministry of Science and Technology (MOST), Taiwan, Republic of China, for financial support under contract number MOST110-2811-E-011-505-MY3.

■ REFERENCES

(1) Nethravathi, C.; Rajamathi, J. T.; Rajamathi, M. Microwave-assisted synthesis of porous aggregates of CuS nanoparticles for sunlight photocatalysis. *ACS omega* **2019**, *4* (3), 4825−4831.

(2) Uesugi, Y.; Nagakawa, H.; Nagata, M. Highly Efficient Photocatalytic Degradation of Hydrogen Sulfide in the Gas Phase Using Anatase/TiO_2 (B) Nanotubes. *ACS omega* **2022**, *7* (14), 11946−11955.

(3) Yang, Y.; Liu, B.; Xu, J.; Wang, Q.; Wang, X.; Lv, G.; Zhou, J. The Synthesis of h-BN-Modified Z-Scheme WO_3/g-C_3N_4 Heterojunctions for Enhancing Visible Light Photocatalytic Degradation of Tetracycline Pollutants. *ACS omega* **2022**, *7* (7), 6035−6045.

(4) Ghobadifard, M.; Mohebbi, S.; Radovanovic, P. V. Selective oxidation of alcohols by using $CoFe_2O_4$/Ag_2MoO_4 as a visible-light-driven heterogeneous photocatalyst. *New J. Chem.* **2020**, *44* (7), 2858−2867.

(5) Kohantorabi, M.; Hosseinifard, M.; Kazemzadeh, A. Catalytic activity of a magnetic Fe_2O_3@$CoFe_2O_4$ nanocomposite in peroxymonosulfate activation for norfloxacin removal. *New J. Chem.* **2020**, *44* (10), 4185−4198.

(6) Motora, K. G.; Wu, C.-M.; Chala, T. F.; Chou, M.-H.; Kuo, C.-F. J.; Koinkar, P. Highly efficient photocatalytic activity of Ag_3VO_4/$WO_{2.72}$ nanocomposites for the degradation of organic dyes from the ultraviolet to near-infrared regions. *Appl. Surf. Sci.* **2020**, *512*, 145618.

(7) Motora, K. G.; Wu, C.-M.; Naseem, S. Magnetic recyclable self-floating solar light-driven $WO_{2.72}$/Fe_3O_4 nanocomposites immobilized by Janus membrane for photocatalysis of inorganic and organic pollutants. *J. Ind. Eng. Chem.* **2021**, *102*, 25−34.

(8) Wang, H.; Yuan, X.; Wu, Y.; Zeng, G.; Dong, H.; Chen, X.; Leng, L.; Wu, Z.; Peng, L. In situ synthesis of In_2S_3@ MIL-125 (Ti) core−shell microparticle for the removal of tetracycline from wastewater by integrated adsorption and visible-light-driven photocatalysis. *Appl. Catal.* **2016**, *186*, 19−29.

(9) Motora, K. G.; Wu, C.-M.; Xu, T.-Z.; Chala, T. F.; Lai, C.-C. Photocatalytic, antibacterial, and deodorization activity of recycled triacetate cellulose nanocomposites. *Mater. Chem. Phys.* **2020**, *240*, 122260.

(10) Purnachander Rao, M.; Wu, J. J.; Asiri, A. M.; Anandan, S. Rice grain like Bi_2S_3 nanorods and its photocatalytic performance. *Mater. Sci. Eng., B* **2021**, *268*, 115144.

(11) Habibi-Yangjeh, A.; Asadzadeh-Khaneghah, S.; Feizpoor, S.; Rouhi, A. Review on heterogeneous photocatalytic disinfection of waterborne, airborne, and foodborne viruses: Can we win against pathogenic viruses? *J. Colloid Interface Sci.* **2020**, *580*, 503−514.

(12) Xu, J.; Hu, C.; Xi, Y.; Wan, B.; Zhang, C.; Zhang, Y. Synthesis and visible light photocatalytic activity of β-$AgVO_3$ nanowires. *Solid State Sci.* **2012**, *14* (4), 535−539.

(13) Huang, C.; Wang, J.; Li, M.; Lei, X.; Wu, Q. Construction of a novel Z-scheme V_2O_5/NH_2-MIL-101(Fe)composite photocatalyst with enhanced photocatalytic degradation of tetracycline. *Solid State Sci.* **2021**, *117*, 106611.

(14) Ming, J.; Liu, N.; Ma, Q.; Sharma, A.; Sun, X.; Kawazoe, N.; Chen, G.; Yang, Y. Bactericidal process and practicability for environmental water sterilization by solar-light-driven Bi_2WO_6-based photocatalyst. *J. Water Process. Eng.* **2022**, *47*, 102713.

(15) Shibu, M. C.; Benoy, M. D.; Shanavas, S.; Haija, M. A.; Duraimurugan, J.; Kumar, G. S.; Ahamad, T.; Maadeswaran, P.; Van Le, Q. White LED active α-Fe_2O_3/rGO photocatalytic nanocomposite for an effective degradation of tetracycline and ibuprofen molecules. *Environ. Res.* **2022**, *212*, 113301.

(16) Chala, T. F.; Wu, C.-M.; Motora, K. G. Rb_xWO_3/Ag_3VO_4 nanocomposites as efficient full-spectrum (UV, visible, and near-infrared) photocatalysis. *J. Taiwan Inst Chem. Eng.* **2019**, *102*, 465−474.

(17) Ademola Bode-Aluko, C.; Pereao, O.; Kyaw, H. H.; Al-Naamani, L.; Al-Abri, M. Z.; Tay Zar Myint, M.; Rossouw, A.; Fatoba, O.; Petrik, L.; Dobretsov, S. Photocatalytic and antifouling properties of electrospun TiO_2 polyacrylonitrile composite nanofibers under visible light. *Mater. Sci. Eng., B* **2021**, *264*, 114913.

(18) Chen, Z.; Cheng, C.; Xing, F.; Huang, C. Strong interfacial coupling for NiS thin layer covered CdS nanorods with highly efficient photocatalytic hydrogen production. *New J. Chem.* **2020**, *44* (44), 19083−19090.
(19) Piranshahi, Z. A.; Behbahani, M.; Zeraatpisheh, F. Synthesis, characterization and photocatalytic application of TiO_2/magnetic graphene for efficient photodegradation of crystal violet. *Appl. Organomet. Chem.* **2018**, *32* (1), No. e3985.
(20) Salimi, M.; Behbahani, M.; Sobhi, H. R.; Gholami, M.; Jafari, A. J.; Kalantary, R. R.; Farzadkia, M.; Esrafili, A. A new nano-photocatalyst based on Pt and Bi co-doped TiO_2 for efficient visible-light photo degradation of amoxicillin. *New J. Chem.* **2019**, *43* (3), 1562−1568.
(21) Salimi, M.; Esrafili, A.; Sobhi, H. R.; Behbahani, M.; Gholami, M.; Farzadkia, M.; Jafari, A. J.; Kalantary, R. R. Photocatalytic Degradation of Metronidazole Using D-g-C_3N_4-Bi_5O_7I Composites Under Visible Light Irradiation: Degradation Product, and Mechanisms. *Chemistry Select* **2019**, *4* (35), 10288−10295.
(22) Pourzad, A.; Sobhi, H. R.; Behbahani, M.; Esrafili, A.; Kalantary, R. R.; Kermani, M. Efficient visible light-induced photocatalytic removal of paraquat using N-doped TiO_2@SiO_2@Fe_3O_4 nanocomposite. *J. Mol. Liq.* **2020**, *299*, 112167.
(23) Abilarasu, A.; Kumar, P. S.; Vo, D.-V. N.; Krithika, D.; Ngueagni, P. T.; Joshiba, G. J.; Carolin, C. F.; Prasannamedha, G. J. Enhanced photocatalytic degradation of diclofenac by $Sn_{0.15}Mn0._{85}Fe_2O_4$ catalyst under solar light. *J. Environ. Chem. Eng.* **2021**, *9* (1), 104875.
(24) Naseem, S.; Wu, C.-M.; Motora, K. G. Novel multifunctional Rb_xWO_3@Fe_3O_4 immobilized Janus membranes for desalination and synergic-photocatalytic water purification. *Desalination* **2021**, *517*, 115256.
(25) Tessema, A. A.; Wu, C.-M.; Motora, K. G.; Naseem, S. Highly-efficient and salt-resistant Cs_xWO_3@g-C_3N_4/PVDF fiber membranes for interfacial water evaporation, desalination, and sewage treatment. *Compos. Sci. Technol.* **2021**, *211*, 108865.
(26) Gu, J.-w.; Guo, R.-t.; Miao, Y.-f.; Liu, Y.-z.; Wu, G.-l.; Duan, C.-p.; Pan, W.-g. Construction of full spectrum-driven Cs_xWO_3/g-C_3N_4 heterojunction catalyst for efficient photocatalytic CO_2 reduction. *Appl. Surf. Sci.* **2021**, *540*, 148316.
(27) Shrisha; Wu, C.-M.; Motora, K. G.; Kuo, D.-H.; Lai, C.-C.; Huang, B.-R.; Saravanan, A. Cesium tungsten bronze nanostructures and their highly enhanced hydrogen gas sensing properties at room temperature. *Int. J. Hydrog. Energy* **2021**, *46* (50), 25752−25762.
(28) Motora, K. G.; Wu, C. M.; Chang, C. C.; Liao, J. H. NIR Light Stimulated Self-Healing Reduced Tungsten Oxide/Polyurethane Nanocomposite Based on the Diels− Alder Reaction. *Macromol. Mater. Eng.* **2021**, *306*, 2100438.
(29) Gong, J.; Xie, Z.; Wang, B.; Li, Z.; Zhu, Y.; Xue, J.; Le, Z. Fabrication of g-C_3N_4-based conjugated copolymers for efficient photocatalytic reduction of U(VI). *J. Environ. Chem. Eng.* **2021**, *9* (1), 104638.
(30) Akhundi, A.; Habibi-Yangjeh, A.; Abitorabi, M.; Rahim Pouran, S. Review on photocatalytic conversion of carbon dioxide to value-added compounds and renewable fuels by graphitic carbon nitride-based photocatalysts. *Catal. Rev. Sci. Eng.* **2019**, *61* (4), 595−628.
(31) Akhundi, A.; Badiei, A.; Ziarani, G. M.; Habibi-Yangjeh, A.; Muñoz-Batista, M. J.; Luque, R. Graphitic carbon nitride-based photocatalysts: Toward efficient organic transformation for value-added chemicals production. *Mol. Catal.* **2020**, *488*, 110902.
(32) Asadzadeh-Khaneghah, S.; Habibi-Yangjeh, A. g-C_3N_4/carbon dot-based nanocomposites serve as efficacious photocatalysts for environmental purification and energy generation: A review. *J. Clean. Prod.* **2020**, *276*, 124319.
(33) Zhang, X.; Wang, X.; Meng, J.; Liu, Y.; Ren, M.; Guo, Y.; Yang, Y. Robust Z-scheme g-C_3N_4/WO_3 heterojunction photocatalysts with morphology control of WO_3 for efficient degradation of phenolic pollutants. *Sep. Purif. Technol.* **2021**, *255*, 117693.
(34) Zhang, Y.; Zhou, J.; Feng, Q.; Chen, X.; Hu, Z. Visible light photocatalytic degradation of MB using UiO-66/g-C_3N_4 heterojunction nanocatalyst. *Chemosphere* **2018**, *212*, 523−532.
(35) Han, C.; Ge, L.; Chen, C.; Li, Y.; Xiao, X.; Zhang, Y.; Guo, L. Novel visible light induced Co_3O_4-g-C_3N_4 heterojunction photocatalysts for efficient degradation of methyl orange. *Appl. Catal.* **2014**, *147*, 546−553.
(36) Li, N.; Fan, H.; Dai, Y.; Kong, J.; Ge, L. Insight into the solar utilization of a novel Z-scheme $Cs_{0.33}WO_3$/CdS heterostructure for UV−Vis-NIR driven photocatalytic hydrogen evolution. *Appl. Surf. Sci.* **2020**, *508*, 145200.
(37) Huang, X.; Liu, J.-X.; Shi, F.; Yu, L.; Liu, S.-H. Ambient pressure drying synthesis of $Cs_{0.33}WO_3/SiO_2$ composite aerogels for efficient removal of Rhodamine B from water. *Mater. Des.* **2016**, *110*, 624−632.
(38) Wu, X.; Yin, S.; Xue, D.; Komarneni, S.; Sato, T. A Cs_xWO_3/ZnO nanocomposite as a smart coating for photocatalytic environmental cleanup and heat insulation. *Nanoscale* **2015**, *7* (40), 17048−17054.
(39) Li, N.; Gao, X.; Fan, H.; Gao, Y.; Ge, L. Insight into the relationship of the high photocatalytic performance and double photochromic activity of Z-scheme Cs_xWO_3/AgBr heterostructures under UV−Vis-NIR light utilization. *Appl. Surf. Sci.* **2020**, *529*, 147038.
(40) Zhu, B.; Xia, P.; Li, Y.; Ho, W.; Yu, J. Fabrication and photocatalytic activity enhanced mechanism of direct Z-scheme g-C_3N_4/Ag_2WO_4 photocatalyst. *Appl. Surf. Sci.* **2017**, *391*, 175−183.
(41) Chen, M.; Guo, C.; Hou, S.; Lv, J.; Zhang, Y.; Zhang, H.; Xu, J. A novel Z-scheme AgBr/P-g-C_3N_4 heterojunction photocatalyst: Excellent photocatalytic performance and photocatalytic mechanism for ephedrine degradation. *Appl. Catal.* **2020**, *266*, 118614.
(42) Huang, J.; Li, D.; Li, R.; Chen, P.; Zhang, Q.; Liu, H.; Lv, W.; Liu, G.; Feng, Y. One-step synthesis of phosphorus/oxygen co-doped g-C_3N_4/anatase TiO_2 Z-scheme photocatalyst for significantly enhanced visible-light photocatalysis degradation of enrofloxacin. *J. Hazard. Mater.* **2020**, *386*, 121634.
(43) Ardani, M. R.; Pang, A. L.; Pal, U.; Zheng, R.; Arsad, A.; Hamzah, A. A.; Ahmadipour, M. Ultrasonic-assisted polyaniline-multiwall carbon nanotube photocatalyst for efficient photodegradation of organic pollutants. *J. Water Process. Eng.* **2022**, *46*, 102557.
(44) Chiam, S.-L.; Pung, S.-Y.; Yeoh, F. Y.; Ahmadipour, M. Highly efficient oxidative degradation of organic dyes by manganese dioxide nanoflowers. *Mater. Chem. Phys.* **2022**, *280*, 125848.
(45) Ahmadipour, M.; Hamzah, A. A.; Pang, A. L.; Thi Le, A.; Chiam, S.-L.; Ahmad, Z. A.; Rajitha, B.; Pung, S. Y. Photodegradation of rhodamine B-dye pollutant using $CaCu_3Ti_4O_{12}$-multiwall carbon nanotube nanocomposites. *J. Environ. Chem. Eng.* **2021**, *9* (3), 105185.
(46) Bekena, F. T.; Kuo, D.-H.; Kebede, W. L. Universal and highly efficient degradation performance of novel $Bi_2(O,S)_3/Mo(O,S)_2$ nanocomposite photocatalyst under visible light. *Sep. Purif. Technol.* **2020**, *247*, 117042.
(47) Khasawneh, O. F. S.; Palaniandy, P.; Ahmadipour, M.; Mohammadi, H.; Bin Hamdan, M. R. Removal of acetaminophen using Fe_2O_3-TiO_2 nanocomposites by photocatalysis under simulated solar irradiation: Optimization study. *J. Environ. Chem. Eng.* **2021**, *9* (1), 104921.
(48) Chiam, S.-L.; Soo, Q.-Y.; Pung, S.-Y.; Ahmadipour, M. Polycrystalline TiO_2 particles synthesized via one-step rapid heating method as electrons transfer intermediate for Rhodamine B removal. *Mater. Chem. Phys.* **2021**, *257*, 123784.
(49) Ahmadipour, M.; Arjmand, M.; Thirmizir, M. Z. A.; Le, A. T.; Chiam, S. L.; Pung, S.-Y. Synthesis of core/shell-structured $CaCu_3Ti_4O_{12}/SiO_2$ composites for effective degradation of rhodamine B under ultraviolet light. *J. Mater. Sci. Mater. Electron.* **2020**, *31* (22), 19587−19598.
(50) Ahmadipour, M.; Arjmand, M.; Ahmad, Z. A.; Pung, S.-Y. Photocatalytic Degradation of Organic Dye by Sol−Gel-Synthesized

https://doi.org/10.1021/acsomega.2c03675
ACS Omega 2022, 7, 38475−38486

$CaCu_3Ti_4O_{12}$ Powder. *J. Mater. Eng. Perform.* **2020**, *29* (3), 2006−2014.
(51) Ahmadipour, M.; Arjmand, M.; Qurratu Aini Abd Aziz, S. N.; Chiam, S. L.; Ahmad, Z. A.; Pung, S.-Y. Influence of annealing temperature on morphological and photocatalytic activity of sputter-coated $CaCu_3Ti_4O_{12}$ thin film under ultraviolet light irradiation. *Ceram. Int.* **2019**, *45* (16), 20697−20703.
(52) Tang, R.; Gong, D.; Deng, Y.; Xiong, S.; Zheng, J.; Li, L.; Zhou, Z.; Su, L.; Zhao, J. π-π stacking derived from graphene-like biochar/g-C_3N_4 with tunable band structure for photocatalytic antibiotics degradation via peroxy monosulfate activation. *Hazard. Mater.* **2022**, *423*, 126944.
(53) Chen, Y.; Zhu, G.; Hojamberdiev, M.; Gao, J.; Zhu, R.; Wang, C.; Wei, X.; Liu, P. Three-dimensional Ag_2O/Bi_5O_7I p−n heterojunction photocatalyst harnessing UV−vis−NIR broad spectrum for photodegradation of organic pollutants. *J. Hazard. Mater.* **2018**, *344*, 42−54.
(54) Bekena, F. T.; Kuo, D.-H.; Kebede, W. L. Universal and highly efficient degradation performance of novel $Bi_2(O,S)_3/Mo(O,S)_2$ nanocomposite photocatalyst under visible light. *Sep. Purif. Technol.* **2020**, *247*, 117042.
(55) Chen, C.; Li, M.; Jia, Y.; Chong, R.; Xu, L.; Liu, X. Surface defect-engineered silver silicate/ceria pn heterojunctions with a flower-like structure for boosting visible light photocatalysis with mechanistic insight. *J. Colloid Interface Sci.*, **2020**, *564*, 442−453.
(56) Ren, X.; Zhang, X.; Guo, R.; Li, X.; Peng, Y.; Zhao, X.; Pu, X. P. Hollow mesoporous g-C_3N_4/Ag_2CrO_4 photocatalysis with direct Z-scheme: Excellent degradation performance for antibiotics and dyes. *Sep. Purif. Technol.* **2021**, *270*, 118797.
(57) Motora, K. G.; Wu, C.-M. Magnetically separable highly efficient full-spectrum light-driven $WO_{2.72}/Fe_3O_4$ nanocomposites for photocatalytic reduction of carcinogenic chromium (VI) and organic dye degradation. *J. Taiwan Inst Chem. Eng.* **2020**, *117*, 123−132.
(58) Palanisamy, G.; Bhuvaneswari, K.; Chinnadurai, A.; Bharathi, G.; Pazhanivel, T. Magnetically recoverable multifunctional ZnS/Ag/$CoFe_2O_4$ nanocomposite for sunlight driven photocatalytic dye degradation and bactericidal application. *J. Phys. Chem. Solids* **2020**, *138*, 109231.
(59) Singla, S.; Sharma, S.; Basu, S. P. MoS_2/WO_3 heterojunction with the intensified photocatalytic performance for decomposition of organic pollutants under the broad array of solar light. *J. Clean. Prod.* **2021**, *324*, 129290.
(60) Samanta, D.; Chanu, T. I.; Basnet, P.; Chatterjee, S. J. Organic dye degradation under solar irradiation by hydrothermally synthesized ZnS nanospheres. *J. Mater. Eng. Perform.*, **2018**, *27* (6), 2673−2678.
(61) Xiong, T.; Ye, Y.; Luo, B.; Shen, L.; Wang, D.; Fan, M.; Gong, Z. Facile fabrication of 3D TiO_2-graphene aerogel composite with enhanced adsorption and solar light-driven photocatalytic activity. *Ceram. Int.* **2021**, *47* (10), 14290−14300.
(62) Ji, Z.; Callahan, D. M.; Ismail, M. N.; Warzywoda, J.; Sacco, A. Development and characterization of a titanosilicate ETS-10-coated optical fiber reactor towards the photodegradation of methylene blue. *J. Photochem. Photobiol.* **2011**, *217* (1), 22−28.
(63) Ramanathan, S.; Moorthy, S.; Ramasundaram, S.; Rajan, H. K.; Vishwanath, S.; Selvinsimpson, S.; Durairaj, A.; Kim, B.; Vasanthkumar, S. Grape Seed Extract Assisted Synthesis of Dual-Functional Anatase TiO_2 Decorated Reduced Graphene Oxide Composite for Supercapacitor Electrode Material and Visible Light Photocatalytic Degradation of Bromophenol Blue Dye. *ACS Omega* **2021**, *6* (23), 14734−14747.
(64) Dalponte Dallabona, I.; Mathias, Á. L.; Jorge, R. M. M. A new green floating photocatalyst with Brazilian bentonite into TiO_2/alginate beads for dye removal. *Colloids Surf. A Physicochem. Eng. Asp.* **2021**, *627*, 127159.
(65) Yu, X.; He, J.; Zhang, Y.; Hu, J.; Chen, F.; Wang, Y.; He, G.; Liu, J.; He, Q. Effective photodegradation of tetracycline by narrow-energy band gap photocatalysts La_2-xSrxNiMnO$_6$ (x = 0, 0.05, 0.10, and 0.125). *J. Alloys Compd.* **2019**, *806*, 451−463.
(66) Lu, Q.; Dong, C.; Wei, F.; Li, J.; Wang, Z.; Mu, W.; Han, X. Rational fabrication of Bi_2WO_6 decorated TiO_2 nanotube arrays for photocatalytic degradation of organic pollutants. *Mater. Res. Bull.* **2022**, *145*, 111563.
(67) Cao, J.; Yang, Z.-h.; Xiong, W.-p.; Zhou, Y.-y.; Peng, Y.-r.; Li, X.; Zhou, C.-y.; Xu, R.; Zhang, Y.-r. One-step synthesis of Co-doped UiO-66 nanoparticle with enhanced removal efficiency of tetracycline: Simultaneous adsorption and photocatalysis. *Chem. Eng. Sci.* **2018**, *353*, 126−137.
(68) Han, W.; Wu, T.; Wu, Q. I. Fabrication of WO_3/Bi_2MoO_6 heterostructures with efficient and highly selective photocatalytic degradation of tetracycline hydrochloride. *J. Colloid Interface Sci.* **2021**, *602*, 544−552.
(69) Nasseh, N.; Barikbin, B.; Taghavi, L. Innovation, Photocatalytic degradation of tetracycline hydrochloride by $FeNi_3/SiO_2/CuS$ magnetic nanocomposite under simulated solar irradiation: Efficiency, stability, kinetic and pathway study. *Environ. Technol. Innov.* **2020**, *20*, 101035.
(70) Tang, R.; Gong, D.; Deng, Y.; Xiong, S.; Zheng, J.; Li, L.; Zhou, Z.; Su, L.; Zhao, J. π-π stacking derived from graphene-like biochar/g-C_3N_4 with tunable band structure for photocatalytic antibiotics degradation via peroxymonosulfate activation. *J. Hazard. Mater.* **2022**, *423*, 126944.
(71) Sakthivel, S.; Neppolian, B.; Shankar, M. V.; Arabindoo, B.; Palanichamy, M.; Murugesan, V. Solar photocatalytic degradation of azo dye: comparison of photocatalytic efficiency of ZnO and TiO_2. *Sol. Energy Mater. Sol. Cells* **2003**, *77* (1), 65−82.
(72) Taghavi Fardood, S.; Moradnia, F.; Forootan, R.; Abbassi, R.; Jalalifar, S.; Ramazani, A.; Sillanpää, M. Facile green synthesis, characterization and visible light photocatalytic activity of $MgFe_2O_4$@$CoCr_2O_4$ magnetic nanocomposite. *J. Photochem. Photobiol.* **2022**, *423*, 113621.
(73) Moradnia, F.; Ramazani, A.; Fardood, S. T.; Gouranlou, F. A novel green synthesis and characterization of tetragonal-spinel $MgMn_2O_4$ nanoparticles by tragacanth gel and studies of its photocatalytic activity for degradation of reactive blue 21 dye under visible light. *Mater. Res. Express* **2019**, *6* (7), 075057.
(74) Arabpour, N.; Nezamzadeh-Ejhieh, A. Modification of clinoptilolite nano-particles with iron oxide: Increased composite catalytic activity for photodegradation of cotrimaxazole in aqueous suspension. *Mater. Sci. Semicond Process* **2015**, *31*, 684−692.
(75) Ahmad, M.; Qureshi, M. T.; Rehman, W.; Alotaibi, N. H.; Gul, A.; Abdel Hameed, R. S.; Elaimi, M. A.; Abd el-kader, M. F. H.; Nawaz, M.; Ullah, R. Enhanced photocatalytic degradation of RhB dye from aqueous solution by biogenic catalyst Ag@ZnO. *J. Alloys Compd.* **2022**, *895*, 162636.
(76) Wang, J.; Zhi, D.; Zhou, H.; He, X.; Zhang, D. Evaluating tetracycline degradation pathway and intermediate toxicity during the electrochemical oxidation over a Ti/Ti_4O_7 anode. *Water Res.* **2018**, *137*, 324−334.
(77) Jin, J.; Liu, M.; Feng, L.; Wang, H.; Wang, Y.; Nguyen, T. A.; Wang, Y.; Lu, J.; Li, Y.; Bao, M. 3D Bombax-structured carbon nanotube sponge coupling with Ag_3PO_4 for tetracycline degradation under ultrasound and visible light irradiation. *Sci. Total Environ.* **2019**, *695*, 133694.
(78) Jin, J.; Liu, M.; Feng, L.; Wang, H.; Wang, Y.; Nguyen, T. A. H.; Wang, Y.; Lu, J.; Li, Y.; Bao, M. 3D Bombax-structured carbon nanotube sponge coupling with Ag_3PO_4 for tetracycline degradation under ultrasound and visible light irradiation. *Sci. Total Environ.* **2019**, *695*, 133694.
(79) Manea, Y. K.; Khan, A. M.; Wani, A. A.; Qashqoosh, M. T. A.; Shahadat, M.; Salem, M. A. S. Hydrothermally synthesized mesoporous CS-g-PA@TSM functional nanocomposite for efficient photocatalytic degradation of Ciprofloxacin and treatment of metal ions. *J. Mol. Liq.* **2021**, *335*, 116144.
(80) Chen, F.; Yang, Q.; Wang, Y.; Yao, F.; Ma, Y.; Huang, X.; Li, X.; Wang, D.; Zeng, G.; Yu, H. Efficient construction of bismuth vanadate-based Z-scheme photocatalyst for simultaneous Cr (VI) reduction and ciprofloxacin oxidation under visible light: Kinetics,

https://doi.org/10.1021/acsomega.2c03675
ACS Omega 2022, 7, 38475−38486

degradation pathways and mechanism. *Chem. Eng. J.* **2018**, *348*, 157−170.
(81) Wang, Y.; Zhu, C.; Zuo, G.; Guo, Y.; Xiao, W.; Dai, Y.; Kong, J.; Xu, X.; Zhou, Y.; Xie, A.; Sun, C.; Xian, Q. 0D/2D Co_3O_4/TiO_2 Z-Scheme heterojunction for boosted photocatalytic degradation and mechanism investigation. *Appl. Catal.* **2020**, *278*, 119298.
(82) Lu, Z.; Chen, F.; He, M.; Song, M.; Ma, Z.; Shi, W.; Yan, Y.; Lan, J.; Li, F.; Xiao, P. Microwave synthesis of a novel magnetic imprinted TiO_2 photocatalyst with excellent transparency for selective photodegradation of enrofloxacin hydrochloride residues solution. *Chem. Eng. J.* **2014**, *249*, 15−26.
(83) Qiu, W.; Zheng, M.; Sun, J.; Tian, Y.; Fang, M.; Zheng, Y.; Zhang, T.; Zheng, C. Photolysis of enrofloxacin, pefloxacin and sulfaquinoxaline in aqueous solution by UV/H_2O_2, UV/Fe (II), and UV/H_2O_2/Fe (II) and the toxicity of the final reaction solutions on zebrafish embryos. *Sci. Total Environ.* **2019**, *651*, 1457−1468.

https://doi.org/10.1021/acsomega.2c03675
ACS Omega 2022, 7, 38475−38486